Impacts of Ultraviolet Backgrounds on Circumgalactic Medium Ion Densities

Elias Taira [iD],[1] Claire Kopenhafer [iD],[2, 1] Brian W. O'Shea [iD],[3, 1, 4, 2] Alexis Rollins,[5] Evelyn Fuhrman,[1]
Molly S. Peeples [iD],[6, 7] Jason Tumlinson [iD],[6, 7] and Britton D. Smith [iD][8]

[1]*Department of Physics & Astronomy, 567 Wilson Road, Michigan State University, East Lansing, MI 48824*
[2]*Institute for Cyber-Enabled Research, 567 Wilson Road, Michigan State University, East Lansing, MI 48824*
[3]*Department of Computational Mathematics, Science, & Engineering, Michigan State University, 428 S. Shaw Lane, East Lansing, MI 48824*
[4]*Facility for Rare Isotope Beams, Michigan State University, 640 S. Shaw Lane, East Lansing, MI 48824*
[5]*Department of Physics & Astronomy, Gallalee Hall, University of Alabama, Tuscaloosa, AL 35401*
[6]*Space Telescope Science Institute, 3700 San Martin Dr., Baltimore, MD 21218*
[7]*Center for Astrophysical Sciences, William H. Miller III Department of Physics & Astronomy, Johns Hopkins University, 3400 N. Charles Street, Baltimore, MD 21218*
[8]*Institute for Astronomy, University of Edinburgh, Royal Observatory, EH9 3HJ, UK*

ABSTRACT

[CK: I'll admit I sort of gave up reading the abstract and focused on the text. It's not worth nitpitcking the abstract in my opinion until the rest of the text is more concrete.] Among the many different features that go into simulations of the circumgalactic medium (CGM), the metagalactic ultraviolet background (UVB) plays a significant role in the ionization of different species but is not fully understood. At this point in time, there are a variety of different models that have been created based on the quantity / intensity of different ultraviolet sources (i.e. stars and quasars). In this project, we perform pairwise comparisons of the ionization patterns of four different UVB models, specifically looking at how these models impact the ion column densities of individual gas clouds in the CGM. From our analysis we find evidence that shows UVB models produce significant changes in the ionization, but these differences are specific to the models' design and will require further investigation.

1. INTRODUCTION

Claire's text changes [CK: Claire's notes]

Brian's text is in this color. [BWO: Brian notes look like this]

The circumgalactic medium (CGM) is the diffuse, multiphase medium that surrounds a galaxy. It is typically observed via quasar absorption spectra due to it's overall low surface brightness. Such observations have been gathered in a number of observational surveys, including COS-Halos (Tumlinson et al. (2013)), COS-Burst (**?**), COS CGM Compendium (Lehner et al. (2018)), KODIAQ and KODIAQ Z (Lehner et al. (2014); Lehner et al. (2016), Lehner et al. (2022)), Red Dead Redemption (Berg et al. (2019)), CASBaH (Burchett et al. (2018); Prochaska et al. (2019)), CUBS (Chen et al. (2020)), CGM2 (Wilde et al. (2021)). These surveys have resulted in absorption estimates for a wide range of metal ions which can then be used to extract information about the physical properties of the CGM such as its multiple gas densities, temperatures, and metallicities.

To better understand the history of the CGM and its evolution over time, a large suite of simulations have been developed. This work includes cosmological simulation studies of the CGM absorption structure such as: EAGLE (Wijers et al. (2020)), GIBLE (Ramesh et al. (2024)), Illustris-TNG50 (DeFelippis et al. (2021)), FOGGIE (Zheng et al. (2020)), and Hummels et al. (2013) as well as some idealized simulations: Fielding et al. (2017) and Butsky et al. (2022). It is vital that these experiments study metal ion distributions to effectively compare the results of these simulations with observation.

Conceptually, there are two broad frameworks for connecting absorption spectra with physical gas properties: forward and reverse modeling. Taking the physical properties of the CGM as the underlying "ground truth," reverse modeling must be applied to observations in order to "back out" the underlying gas state from the observed spectra. The absorption spectrum represents a reduced set of information about the system that generated it and such a situation is also known as an "inverse problem." Conversely, efforts to make synthetic observations of simulations are engaging

in forward modeling. Synthetic observations can go as far as generating mock spectra targeting a specific instrument (such as the Hubble Telescope's COS) complete with noise (Hummels et al. (2017)). For spectral observations of metal ions, the two approaches can "meet in the middle" by generating ionic column densities. Column densities must be reversed modeled from spectral line features and forward modeled from bulk gas properties. While simulations could in theory directly model individual metal ion densities—thereby removing the need to forward model ionic column densities—this is computationally intractable. It is already quite uncommon to track individual element densities (the notable exception being EAGLE; Schaye et al. (2014)) much less individual ion densities. Therefore, inferring elemental and ionic gas fractions must be part of the forward modeling process.

Connecting ionic absorption and gas properties through either forward or reverse modeling involves several assumptions. In recent years there has been considerable effort invested in characterizing the uncertainty that these assumptions introduce into reverse modeling. For instance, to extract physical data from absorption spectra, it is commonly assumed that each absorption feature originates from a single gas "cloud" or "clump" along the line of sight. Instead, Haislmaier et al. (2020) showed that multiple line components may be needed to accurately capture the information contained in an absorption feature. Single component analysis is only capable of reproducing the average metallicity of multiphase structures (Marra et al. (2021)) while multiple spatially distinct clumps can contribute to the same absorption feature if they overlap in line-of-sight velocity space (Marra et al. (2022)).

While it is likely not always true, for both forward and reverse modeling it is assumed that CGM gas is in ionization equilibrium; that is, that individual ions are in both collisional and photoionization equilibrium. In particular, the assumption of photoionization equilibrium requires that we understand the nature of the metagalactic ultraviolet background (UVB)—the background radiation originating from quasars and newly-formed stars. However, the UVB is challenging to model as it requires its own broad assumptions about extragalactic star formation rates and the distribution of quasars throughout the universe across cosmic time. Indeed, the UVB itself is an abstraction representing the *average* UV radiation field at a point in space far from any single galaxy. Because of these challenges, many models for the metagalactic UVB have been created over the past few decades. This makes the UVB a potential source of uncertainty in the models that connect spectral observations and their underlying gas.

Again, there has been effort in quantifying how much uncertainty the UVB contributes to the reverse modeling of absorption spectra. Both Gibson et al. (2022) and Acharya & Khaire (2022) have studied how the extreme-UV (EUV) portion of the UVB ($\approx$ 1–1000 Ryd) affects inferences of number density and metallicity. The former finds that hardening the EUV slope from $\alpha_{EUV} = -2.0$ to -1.4. causes the metallicity to increase by an average of 3 dex. The latter found that the number density and metallicity could vary by factors of 6.3 and 3.7 in low density gas ($\approx 10^{-5}$ cm^{-3}) and 3.3 and 2.2 in high density gas ($\approx 10^{-3}$ cm^{-3}).

Though understanding model uncertainty is a necessary process, it is important to reiterate that efforts have so far been focused on the implications for reverse modeling. Forward modeling from simulations is extremely valuable for comparing simulation and observations so it is imperative that we quantify the uncertainty introduced by common, necessary assumptions to the forward modeling process. As a start to this process, the goal of this work is to quantify the variation in absorber column density introduced by changing the UVB. We do this by repeatedly post-processing the FOGGIE cosmological simulations (Peeples et al. (2019), Simons et al. (2020)) with a pipeline that is identical except for the choice of UVB. We then match clumps between each post-processing pass based on their physical location in order to compare the forward modeled column densities and underlying volumetric densities and temperatures. In Section 2, we discuss our data selection, simulation pipeline, and general methodology for performing our analysis, including the algorithm for matching clumps. In Section 3, we present the results of our analysis, and in Section 4, we interpret our findings and discuss the implications of our results in the broader research community. Finally, we summarize our findings and discuss possibilities for future research project in Section 5.

2. METHODOLOGY

For clarity, we present our process in the form of a pipeline in Figure 1. Each block of the figure corresponds to a subsection below. We base our analysis on the FOGGIE simulations (Section 2.1; Peeples et al. (2019), Simons et al. (2020)). We use the Synthetic Absorption Line Surveyor Application (Boyd et al. (2020)) to cast lines of sight or "rays" within a specified range of impact parameters (Section blah). SALSA is built on Trident, a synthetic absorption spectra tool (Hummels et al. (2018)) that is used by SALSA to infer ionic number densities. Trident is itself built on yt (Turk et al. (2011)), which it uses to load the FOGGIE simulation data. The number densities inferred by Trident are used by SALSA to find absorbers within each ray.
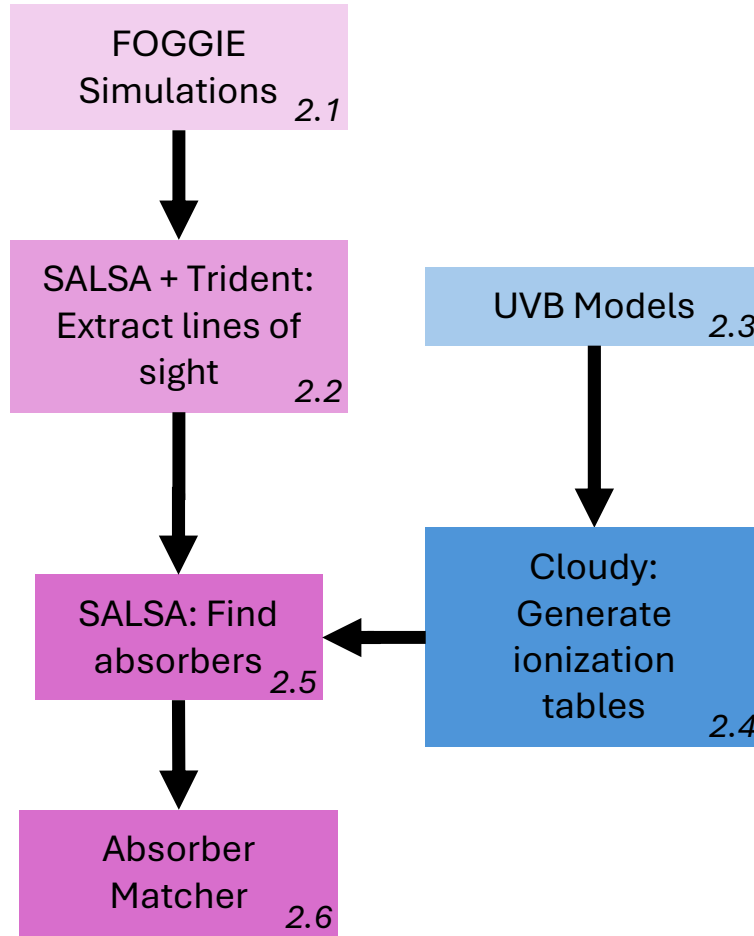
Figure 1: Overview of our analysis pipeline. Each block represents a different calculation and/or data product detailed in the following subsections. In the bottom right corner of each box is the section that each block corresponds to.

We adopt four different UVBs as outlined in Section 2.3 and, using SALSA, find a set of absorbers for each. For each set of SALSA absorbers created from each UVB, we match the absorbers based on their spatial position along the line of sight so that pairwise comparisons can be made.

2.1. *The FOGGIE Simulations*

The FOGGIE (Figuring Out Gas and Galaxies In Enzo) Galaxies are a suite of cosmological zoom-in simulations of Milky Way-like galaxies that were made using Enzo. One defining feature of the FOGGIE simulations is its high resolution of the CGM, allowing for a more thorough analysis of this region. This is also the main reason we selected these galaxies for our study (Peeples et al. (2019), Simons et al. (2020)). We base our analysis on the Hurricane galaxy at redshift 2.5, during cosmic noon when the intensity of UV radiation is very high due to the rapid formation of young stars.

One limitation of the FOGGIE simulations however, is that they only follow the evolution of a single "metal field", in which all of the CGM metals are tracked as one large field, ignoring traces of individual species of ions. This then necessitates some form of post-processing method to extract data for these untracked ions.

2.2. *Extracting Lines of Sight*
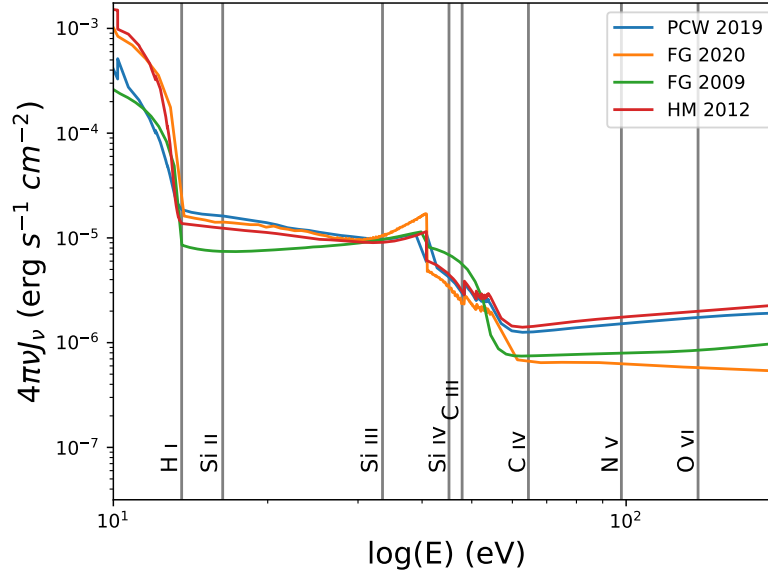
Figure 2: Indicates the energy distribution of two of the newest UVB models at redshift 2.5, FG 2020 and PCW 2019. The x-axis is the energy of the UVB in units of eV and the y-axis is the intensity of the UVB in units of $ergs^{-1}cm^{-2}$. [BWO: Need to tighten up the y-axis and make lines thicker, text larger so it's easy to see. I think we also ought to make a data table with all of this information and make it publicly available – people will really appreciate it and refer to the paper!]

We used SALSA to mimic observations by generating a series of randomly oriented lines of sight, or "rays," through the CGM. SALSA calculates random start and end points for our rays given a central point, ray length, and a range of impact parameters. This lets us approximate observational sightlines passing within a certain distance (i.e., impact parameter) of the galaxy center. [CK: Our central point corresponds to peak of the halo dark matter distribution. What are the values of the length and impact parameter bounds? Claire TODO: report the virial radius of the halo (we want to make it clear that we're actually looking at the CGM, not the ISM or IGM!).] In this way, we generate 100 rays through our simulated galaxies. These same 100 rays will be reanalyzed using different UV backgrounds (Section 2.3.

With the spatial orientation of the rays specified by SALSA, Trident is used to infer the ionic number densities using CLOUDY-generated equilibrium ion fraction tables (see Section 2.4) using the following equation:

$$n_{X_i} = n_X f_{X_i}$$

, where n_X is the total number density of the element as determined by the elemental abundances, which, in the case of this work we elect to use Solar abundance patterns. f_{X_i} is the equilibrium fraction of a given ion, and n_{X_i} represents the inferred ion number density (Hummels et al 2018).

2.3. *UVB Models*

We selected two different "families" of models with two models each for a total of four UVB models in total. These families are Faucher-Giguère et al. from 2009 and 2020 (FG09 and FG20 respectively, and Puchwein et al. 2019 (PW19) and Haart & Madau 2012 (HM12). These models were selected both to allow us to analyze the differences between model families and the differences between model generations. PCW 2019 was developed in response to new photoionization and photoheating rates being determined by (Oñorbe, Hennawi & Lukič, 2017) as well as new calibrations to their effective rates to reach a higher optical depth ($\tau_e = 0.065$) to match the Plank 2015 observations (Faucher-Giguère (2020)). For FG 2020, they make a number of updates based on: updated galaxy UV luminosity functions, a new stellar spectral template, new AGN luminosity functions, improved IGM opacity measurements, updated Ly α forest constraints, Plank 2018 reionization constraints and finally, updated observational constraints on He IIreionization (Faucher-Giguère (2020)).

In Figure 2, we show the intensity spectra (in units of $erg\ s^{-1}\ cm^{-2}$) of all four UVBs that we use in this work. Each of the vertical black lines represents the ionization energies (in eV) of each of the ions used in this study, the list of which is as follows: H I, Si II, Si III, C III, Si IV, C IV, N V, O VI. We include Si II- Si IV to evaluate the effect of the UVB at different ionization states of an element. C III is used as its ionization state is in a region of the spectra that is changing very rapidly, compared to Si IV which has a very similar ionization state, may help reveal the effects of the nonlinear portion of the spectra on column density. As for C IV, N V, and O VI, they are included due to their observational significance. C IV, is useful for tracing CGM cold gas.

2.4. *CLOUDY Ionization Tables*

As seen in Equation 1, the UVB is coupled to the pipeline through equilibrium ionization fractions, f_{X_i}. We use CLOUDY to generate a table of these fractions for a broad range of densities, temperatures, and metallicities. Both the FG09 and HM12 models have ionization fraction tables available as part of the Trident project [1]. The newer FG20 and PW19 models do not have readily available tables made for them. To generate tables for these UVBs, we ran a series of one-zone CLOUDY models to determine the equilibrium ionization fractions for selected elements (see Section 2.3 for list). These models include self-shielding and were coordinated using the same code as the older FG09 and HM12 models [2] . [CK: Britton's Cloudy Cooling Tools are not widely known nor do they have a reference, so we don't need to name drop them. Including a footnote with the github link is good though.]

2.5. *Absorber Extraction*

Once Trident has inferred ionic number densities using the CLOUDY ionization fraction table corresponding to one of our four UVBs, SALSA is able to identify absorbers within the rays it randomly placed (Section **??**). SALSA does this iteratively each individual ion using the Simple Procedure for Iterative Cloud Extraction (SPICE) method. A key assumption of this algorithm is that regions of high column density should give rise to detectable absorption features. This algorithm works by setting a number density threshold above which lies some fraction of the ray's total column density. By default, the cutoff is 0.8 Then, bounds are set that define distinct "clumps" of gas that fall above this cutoff. That is, regions of space are identified that account for 80% of the total column density of the line. On the next pass, additional regions are flagged that account for 80% of the column density that remains unaccounted for after the first pass. Clumps from each pass are combined if their average line of sight velocities are within 10 km/s of each other. This process is repeated until the column density of the remaining data that has not been assigned to an absorber is below the minimum density threshold. Therefore, the SPICE algorithm is controlled by two free parameters: the cutoff fraction and the minimum column density.

To ensure our results are not sensitive to these two free parameters, we employ a pseudo-grid search to determine the optimal set of parameters to apply to this algorithm. We track the distribution of $\log(N_{\text{H I}})$ for absorbers found by independently varying both parameters. The parameter not being analyzed is left at its default setting (0.8 for the cutoff fraction and 10^{13} cm^{-2} for the minimum column density). It should be noted that we did not investigate the non-linear effects from varying both settings at once. Our aim is to find a parameter space in which we find a "stable" region in parameter-space in which the distribution does not shift significantly between different parameter settings.

Figure 3, we plotted a histogram showing H I column densities of SALSA absorbers for two different SALSA settings: cutoff fraction (Fig. 3a) and minimum density (Fig. 3b). For our cutoff fraction distributions in Fig. 3a, we select four different settings including the default fraction of 0.8, from 0.6-0.9 in intervals of 0.1 while the minimum density cutoff remains at $log(N) = 13\ cm^{-2}$. In Fig. 3b, the minimum column density cutoff is plotted at four different settings, including the default minimum column density setting, ranging from $\log(N) = 11$–14 in intervals of $\log(N) = 1$.

From our variation of the cutoff fraction in panel (a) of Figure 3, we find that the overall distribution remains generally consistent despite the different settings used. Even though the total number of absorbers that SALSA identifies steadily decreases with increasing cutoff fraction, this decrease is small relative to the total number of absorbers found. This indicates that the cutoff fraction does not have a significant impact on the results of our analysis, so we elected to leave this parameter at its default value of 80%. In panel (b) of Figure 3, we see that as the minimum column density parameter increases, the total number of absorbers detected decreases rapidly, with the overall H I column density distribution skewing towards higher column densities. Unlike with the cutoff fraction, the H I column density distribution does not remain stable as we vary the minimum column density. Instead, we chose to

---

[1] https://trident-project.org/data/ion_table/

[2] https://github.com/brittonsmith/cloudy_cooling_tools

UVB Number Density Comparison H I (a)

UVB Number Density Comparison H I (b)
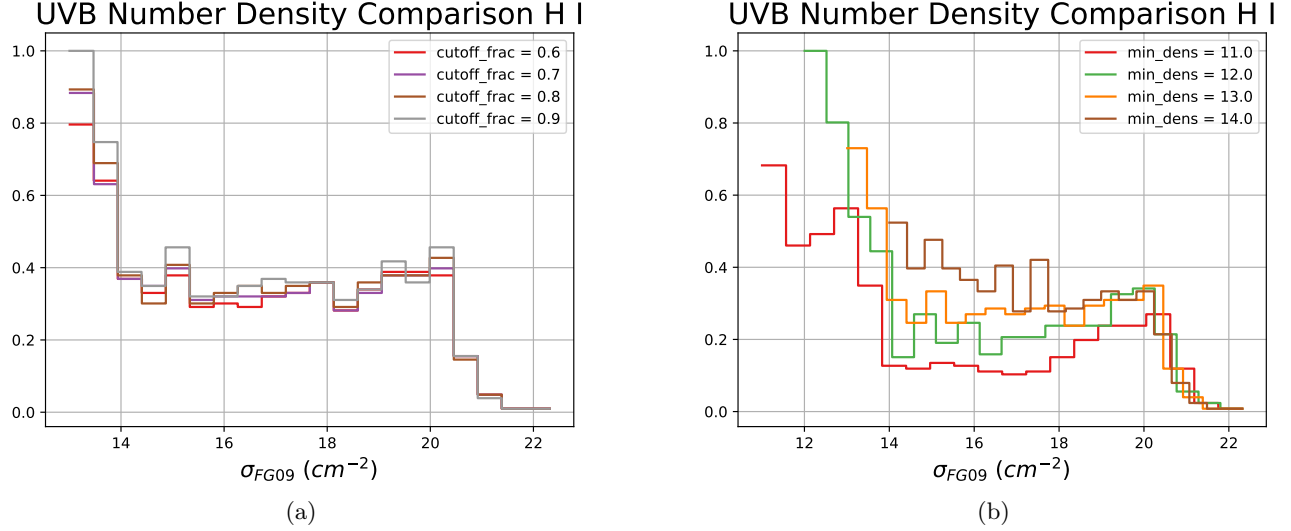
Figure 3: (a) A histogram showing the column density of SALSA absorbers produced using the SPICE method with cutoff fractions from 0.6–0.9 in intervals of 0.1. (b) A histogram of SALSA absorbers produced at different minimum density thresholds from $\log(N) = 11$–14 in intervals of $\log(N) = 1$.

adopt different minimum column densities for each ion of interest. For H I, C III, C IV, and O VIwe use $log(N) = 12.5$. For Si IIand Si III, we use $log(N) = 11.5$. Finally, for N V, we use $log(N) = 13.0$. We select these values based on the minimum column density these absorbers could potentially be detected by observation (Tumlinson et al. (2011), Tumlinson et al. (2013), Werk et al. (2013), Werk et al. (2016), Bordoloi et al. (2014), Bordoloi & Longmire (2018)), Lehner & Howk (2011))

Once SALSA has identified absorbers for each ion based on their number density, it reports gas properties such as volumetric density, temperature, and metallicity for each absorber. These quantities are a column-density weighted average of the cells belonging to that absorber.

2.6. *Absorber Matching*

The UVB will affect the ionic number densities of the ray and therefore the clumps identified by the iterative SPICE algorithm. Once the SPICE algorithm has been run on our 100 rays for each of our four UVBs, we must match absorbers based on their position along their lines of sight. This is because our analysis relies on pairwise comparison between absorbers from different UVBs. Altering the UVB and overall ionic number density can change the shape of the identified absorbers, so we categorize them into different groups based on their relative size and position along a given ray. The categories are as follows:

1. Match: absorbers are of the exact same size and position along the ray, covering the same simulation cells

2. Different Size: the two absorbers are different sizes (i.e., they span a differing number of simulation cells) but match in either start or end position. In other words, one UVB results in a clump that is longer or shorter than that from another UVB, but they still occupy the same physical region along the ray.

3. Overlap: absorbers have a significant overlap with one another along the line of sight, but they do not line up in terms of size or position (i.e. they do not share a start or end point and may encompass a differing number of cells).

4. Merge: when one of the UVBs produces multiple small absorbers but the other UVB produces only one large absorber that is a superset of the smaller ones

5. Lonely: there exists an absorber in one UVB while the other UVB has no absorber
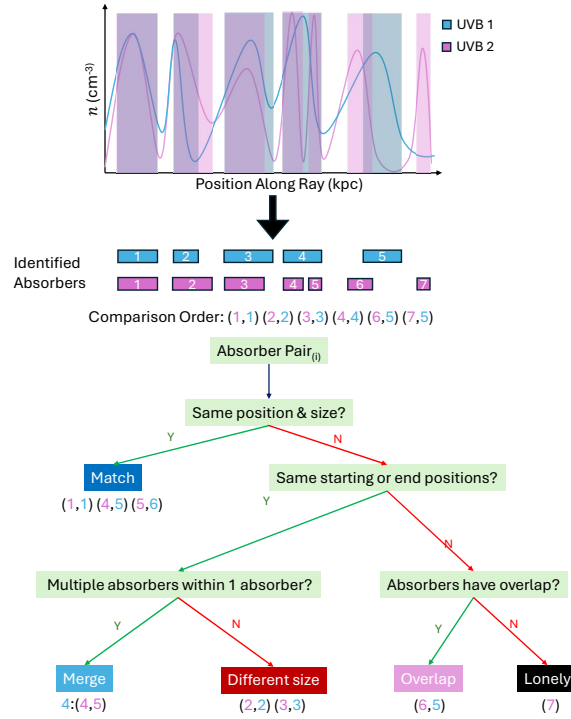
Figure 4: Diagram showing a flow chart of how the pairwise comparison algorithm. Each absorber is numerically labled in the order they appear along the ray. The "comparison order" list indicates the order in which pairs of absorbers are put through the flow chart.

All of these comparisons are made using a series of boolean logic with some margin of error allotted. We apply a margin of error in this case to prevent situations in which compared absorbers are misclassified. Specifically, this is to prevent situations in which, for example, a pair of absorbers would fall into the Different Size category when the size of the two absorbers is only a one-cell difference. It is also to prevent situations in which absorbers would be classified as Lonely when the two absorbers are only a few cells apart from one another, and still viable for comparison.

Specifying a margin of error in terms of cells is difficult for this analysis as the ray can have a variable pathlength dl through each cell, even if those cells have uniform spatial resolution. To address this issue, we have decided to adjust the margin of error, such that it has the lowest number of absorber pairs that are classified as 'match' that exist outside the general trend of the data This hinges on the assumption that absorbers that share similar spatial coordinates have similar physical quantities (gas density and temperature). Using this method, we found that 7 simulation cells along the line of sight was the optimal margin of error.

In order to compare absorber properties across UVBs, the small individual clumps in merge cases had their properties combined in linear space. As for the other physical quantities of the absorber such as temperature and gas density (see Section 2.5) these were combined by weighted average based on the column densities of the individual absorbers in the following equation:

$$\frac{x \cdot \sigma}{\sum_{i=1}^{n} N_i}$$

where n is the number of absorbers within the set being combined, x is the array of a given physical quantities of length n, and σ is the array column densities also of length n

Lonely cases were removed from the analysis as they have no partner to compare to. We found that the number of such absorbers was small. The number of lonely absorbers is 1% for each pairwise comparison
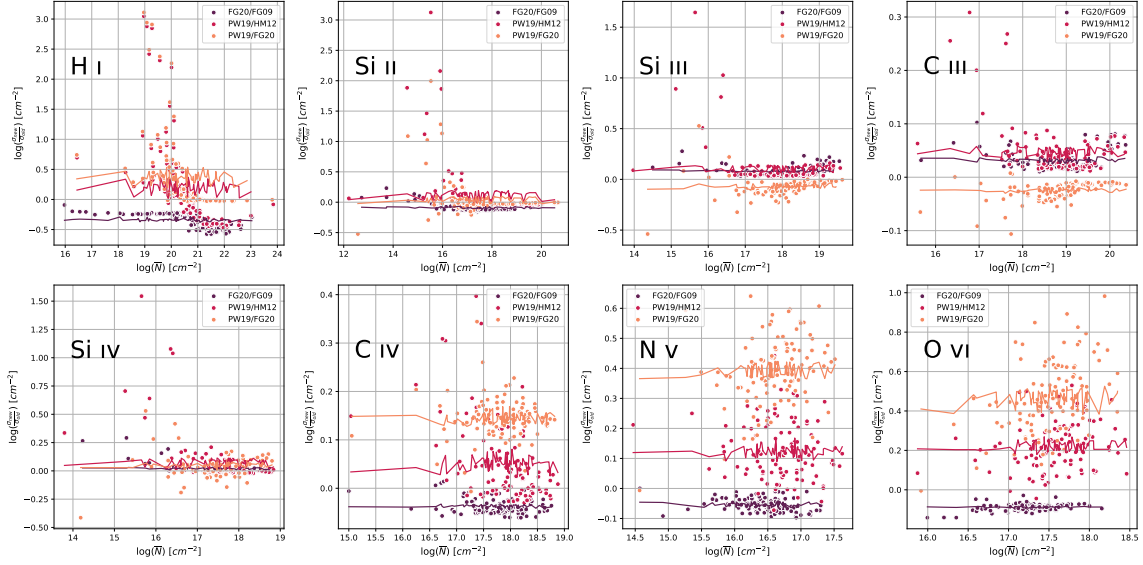
Figure 5: Differences in total column density along the line of sight as different UVBs are applied. Differences are quantified as $\log(N_{\mathrm{new}}/N_{\mathrm{old}})$, the ratio between new and old UVBs as listed in the figure legend. Quantities on the x-axis are the average of the total column densities between the two UVBs in the comparison (written $\log(\bar{N})$). The points in purple refer to the comparison between FG20 and FG09 ($\log\frac{FG20}{FG09}$), the magenta points refer to PW19 and HM12 ($\log\frac{PW19}{HM12}$), and the orange to PW19 and FG20 ($\log\frac{PW19}{FG20}$). Additionally, there is also a line plotted for each comparison indicating the moving average of the data with a window size of 20 rays. The different ions used in the comparison are ordered in terms of increasing ionization energies from left to right.

Additionally, there were a few rays for which the sorting algorithm was unable to categorize absorber pairs. These cases consisted of absorbers that fell into multiple categories, or rays that had no absorbers. [CK: Is this because of our margin of error? I would otherwise think our categories are mutually exclusive.] Instead of handling all of these outliers, the rays are removed from the analysis. The number of removed rays tends to stay around 0-10% for most ions. However for N V, 37-68% are removed from the analysis. This is mostly due to the fact that the abundances of nitrogen are significantly lower than the other ions used in this work. Thus, for SALSA recognized many of these rays as having no observable absorbers.

[CK: Once you make the table of total absorber counts for each UVB, describe it and reference in a paragraph here, at the end of this subsection]

3. RESULTS

Using the methodology laid out in Section 2, we make three pairwise comparisons: FG09 and FG20 (Faucher-Giguère family), HM12 and PW19 (Haardt-Madau-Puchwein family), and finally FG20 and PW19, the latest models from each family. We begin by comparing the total column densities along each ray, then performing a comparison between individual absorbers and their physical properties as identified by the pipeline laid out in Section 2

Figure 5 shows a comparison between the total column densities between each of the three pairwise model comparisons, plotting the average $\bar{N}$ in the x-axis, along with the log difference between the two UVBs in the y-axis. The points in purple refer to the comparison between FG20 and FG09 ($\log\frac{FG20}{FG09}$), the magenta points refer to PW19 and HM12 ($\log\frac{PW19}{HM12}$), and the orange to PW19 and FG20 ($\log\frac{PW19}{FG20}$). Additionally, there is also a line plotted for each comparison indicating the moving average of the data with a window size of 20 rays. The different ions used in the comparison are ordered in terms of increasing ionization energies from left to right.

Throughout each comparison, we find that FG20/FG09 tends to have the most agreement between models with all differences between the two UVBs never being larger than 0.75 for each ion. These differences also tended to be consistent for the entire density range (that is, the scatter would exist entirely above or below the zero-line with very little exception). The PW19/FG20 comparison saw much larger differences. Starting in H Isubfigure (top left), the $\bar{N}$ region between $log\overline{N} = 19 - 20$, the density of H Iin PW19 rays is significantly larger than the HM12 rays up to a factor of 10^3. In the Si IIsubfigure, there is a similar feature from $log\overline{N} = 14 - 16$. However this appears to be

significantly less dense than in the feature in H I, and in Si IIIand Si IV, this feature appears to be even less consistent, and only reaches extremes of 10³. This feature is also present in the PW19/FG20 comparison in the H Isubfigure, almost perfectly aligning with the P19/HM12 comparison. Unlike P19/HM12, PW19/FG20 this feature is significantly less prevalent in Si IIwith a similar range of $log\overline{N} = 14 - 16$, but only a peak of 10^2. After this ion, this feature does not persist.

Looking at the differences between pairwise comparisons, We find that the distributions fall into three groups:

- H Iand Si IIwith higher column densities in the PW19/HM12 and PW19/FG20 comparisons along with a very strong agreement between their distributions.

- Si III, C IIIand Si IVwhich show stronger agreements between models. That is to say that the N ratios between the different UVBs tend to be closer to 0 compared to the other ions in the analysis

- C IV, N Vand O VIwhere each of the pairwise comparisons fall into distributions that increase in scatter and distance from one another with increasing ionization energy.

Figure 7 shows the column density differences between FG09 and FG20 absorbers and their relationship with different physical quantities. The column density difference is $\log \frac{FG09}{FG20}$. In order from left to right, the quantities are: FG09 absorber column densities (C1), absorber gas density (C2), temperature (C3), and finally a histogram of the column densities at the rightmost column. Each row represents a different ion as indicated by the leftmost column.

In H I, we see that FG 2020 has systematically lower column densities than FG 2009. Notably, at gas density $\log n = -1$, the difference between the two UVBs increases to a maximum of 0.5 dex. This difference appears to be associated with lower temperature absorbers ($\log(T)$ =4-4.5 K) as evidenced by C3. In fact, most of the H Iabsorbers with larger FG09 column densities, tend to be associated with densities lower than $\log(T)$ =5 K.

Si II, Si III, C III, Si IVand C IVall have very similar trends to one another, at ¡ $\log \overline{n} = -4$, FG20 tends to have higher densities that has a downward trend towards until $\log \overline{n} = -4$ after which, the UVB absorbers have similar column densities, staying around 0. Si II, while mostly following these trends, appears to be shifted downwards by 0.125 dex. In some of the other lower ionization-state ions, Si IIIand C III, we see that around $\log \overline{n} = -3$, there is an upwards trend where FG20 has higher column densities. The density remains around 0 in Si IVand C IV. There are no noticeable trends with temperature except for C IV, where FG20 tends to have higher densities at ¿$\log \overline{T} = 4.625$

N Vis very sparse, and is very difficult to extract a trend from, however it does appear that the absorbers SALSA does identify have very similar column densities to one another. There is a faint trend with $\overline{T}$ where ¿$\log \overline{T} = 4.6$ tends to have more similar column densities as temperature increases.

O VIhas no trends with gas density or temperature, but FG09 does have systematically higher column densities by a factor of 0.1 dex.

Fig. 8 is a very similar plot to Fig. 7 now with the comparison being between PW19 and HM12 with the column density ratio being $\sigma_{PW19}/\sigma_{HM12}$.

In H I, we see from $\log \overline{n} = -4$ to -1.5, we see that there are significant differences between the two UVBs with PW19 absorbers having column densities larger by 4 dex. Based on C1, these differences correspond with HM12 absorbers with lower column densities. In C3, these absorbers have $\log \overline{T} > 4.25$.

Excluding Si II, which does not appear to have many significant differences between the two UVBs, the Si and C ions both show significant column density differences at $\log \overline{n} < -4$ after which, the column density differences tend to stay around 0. While Si ion column density differences become less significant with increasing $\overline{n}$, C ion column densities with $\log \overline{n} = -4.25$ have larger column density differences peaking at 0.5 dex for C IIIand 0.75 dex for C IV.

As with Fig. 7, N Vis very sparse and thus it is very difficult to extract any useful information from these figures.

O VIhas an interesting trend with gas density. At $\log \overline{n} = -4.5$, the column density difference immediately scatters with many PW19 absorbers having significantly larger differences ranging from 0 to 0.6 dex. There are no notable trends with HM12 column density or $\overline{T}$.

Fig. 9 is similar to the previous two figures (Fig. 7 and Fig. 8), now comparing PW19 and FG20 with a density ratio of $\sigma_{PW19}/\sigma_{FG20}$.

H Ihas a similar feature to Fig. 8 from $\log \overline{n} = -4$ to -1.5, also peaking around 4 dex. This structure is also reflected in C3 in which the absorbers with larger column density differences exist at $\log \overline{T} > 4.25$.
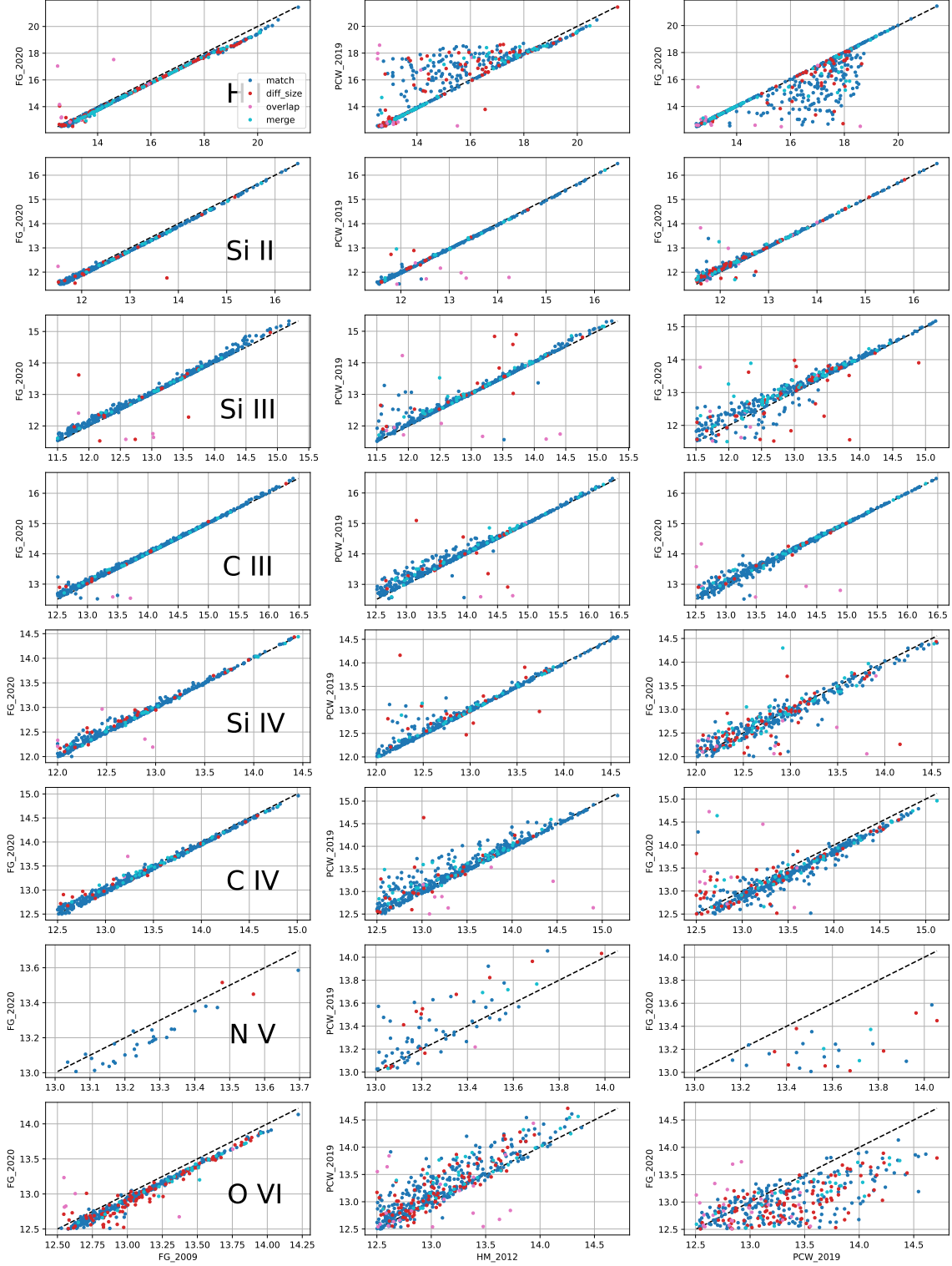
Figure 6: Direct absorber comparison of column for each pairwise comparisons for each ion in the analysis. The x-axis contains the log column density for absorbers in the older UVB models, while the y-axis contains log column densities of the newer models. The dashed black line at the center of the figure indicates the line of equality between the to models. The pairwise comparisons going from left to right are: FG20 vs FG09, PW19 vs HM12 and FG20 vs PW19. This figure's new, so I haven't began discussing it yet.
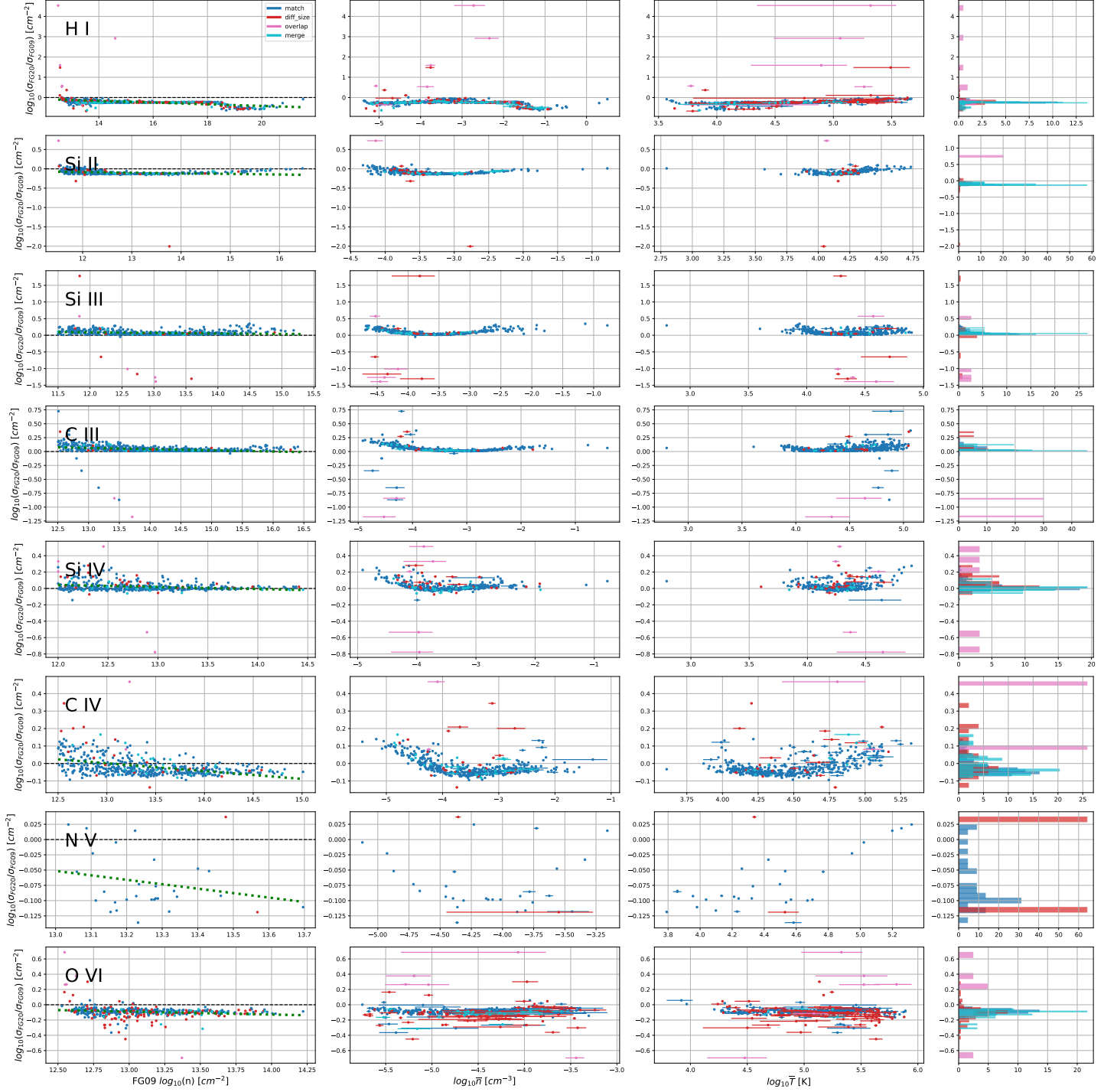
Figure 7: Comparison between the SALSA absorbers from the FG 2009 and FG 2020 UVB models based on their column density, temperature and gas density. The leftmost column is a direct comparison between column densities with FG 2009 column densities in the x-axis and FG 2020 in the y-axis. A dashed black line is included to represent the "match" line where the two absorber column densities match with one another. Additionally, a green dotted line is included as a linear fit generated to the comparison scatter. In the next column to the right is the gas density comparison where the x-axis is the average gas density (n) between the two UVB models with errorbars showing the lower and higher densities. In the y-axis is the $\log_{10}$ ratio between FG20 / FG09. The third column is the temperature comparison where the x-axis is the average temperature with errorbars showing the smaller and larger values of temperature and the y-axis is once again the $\log_{10}$ ratio between FG 2020 / FG 2009. The final column is a histogram showing the distriubtion of the FG 2020 - FG 2009 ratio. Each row is a different ion used in the analysis, and each point is colored based on their spatial relation to one another as outlined in section 2.6.
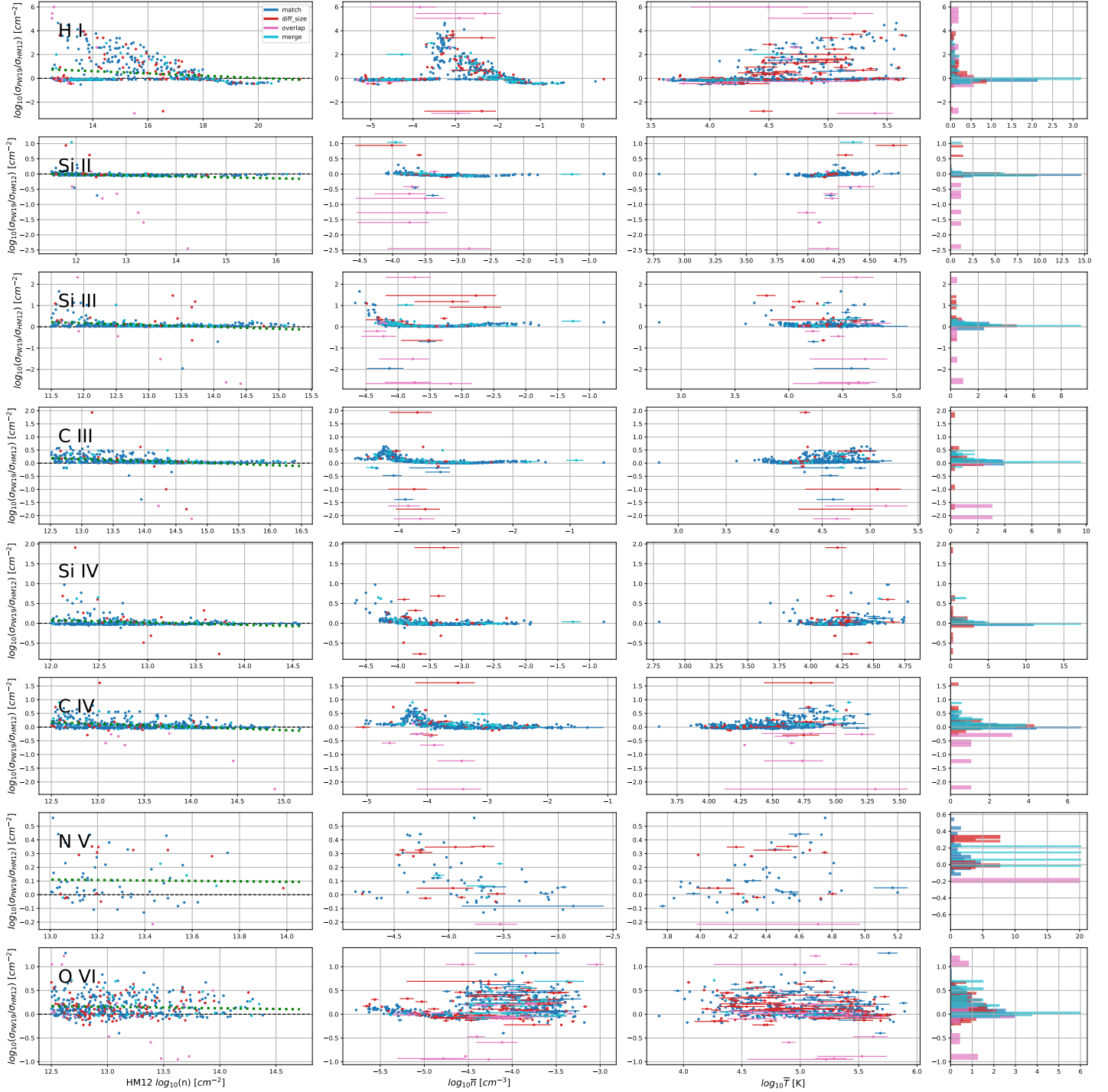
Figure 8: Similar to Fig. 7, now comparing HM12 and PW19. The ratio between the two is $\sigma_{PW19}/\sigma_{HM12}$.

Si III, C III, Si IV and C IV, like Fig. 8 have very little column density difference except for $\log \overline{n} < -4$ where differences become significantly larger. N V is very sparse and difficult to parse. O VI has overall very high scatter, but it does appear that as gas density increases, the column density difference grows larger in favor of PW19.

It should also be noted that in addition to σ and n we also tested metalicity (Z) to see if we could find any relationships with the absorber column density ratios, however, we did not find any correlation between any of the ions we tested.
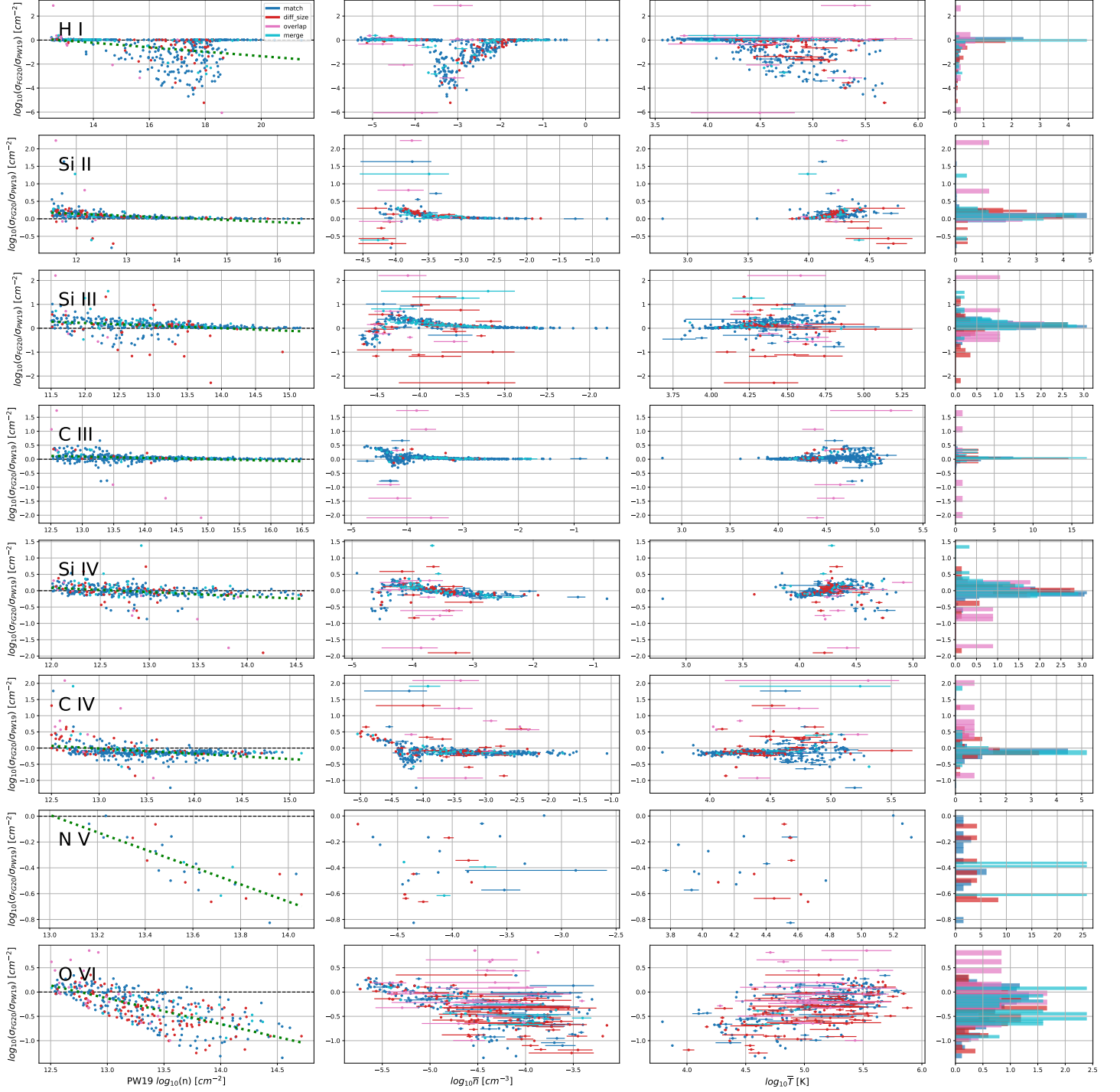
Figure 9: Similar to Fig. 7 and Fig. 8, now comparing FG20 and PW19. The ratio between the two is $\sigma_{PW19}/\sigma_{FG20}$.

4. DISCUSSION

Thus far, we have utilized SALSA to create and analyze 100 randomly-oriented rays through a simulated FOGGIE galaxy, to extract absorbers from each ray under four different UVBs (FG09, FG20, HM12 and PW19). We then performed three pairwise comparisons (FG09 to FG20, HM12 to PW19 and PW19 to FG20) for eight different ions (H I, Si II, Si III, C III, Si IV, C IV, N V, O VI). Here we made a figure plotting the total column density ratio plotted

the column density ratios ($\sigma_{FG20}/\sigma_{FG09}$, $\sigma_{PW19}/\sigma_{HM12}$, $\sigma_{PW19}/\sigma_{FG20}$ respectively) against three different quantities: column densities of the older UVB, $\overline{n}$ and $\overline{T}$.

4.1. *Summary of Results*

For our initial total column density comparison in fig. 5, we find that the data is not in agreement with the intensities of the UVB at different energies as shown in Fig. 2. This is especially evident with H Iwhere in Figure 2 we see a distinct difference between the newer and older generations' intensity at 1 Ryd. The newer models have higher intensities than the older models. Unlike our expectations, we see in Fig 5, FG09 has higher column densities than FG20, and PW19 has higher total column densities than both HM12 and FG20 by up to 3 dex.

For the SALSA-extracted absorber pairs (fig 7-9), we find that our results are physically viable. [CK: This is too vague of a statement. Be more specific; e.g., trends in scattering are consistent with our understanding of photoionization.] The column density ratio scattering tends to increase with increasing ionization energy, which makes sense as ions with larger ionization energies are more difficult to predict with photoionization as collisional ionization begins to dominate. We also find that the vast majority of absorber pairs were classified as "match" and tend to agree very well between the two models being compared in terms of column density, gas density and temperature. The vast majority of outliers that we find do not fall into the match category as the identified absorbers occupy different numbers of cells and positions along the line of sight. While SALSA does complicate this process, we are using the same algorithm across all samples, so this complication is mitigated somewhat. Temperature has noticeably weaker trends with column density, however we still see that the most significant differences occur in regions of higher temperatures while lower temperature regions tend to have more agreement between models. This is likely due to the fact that these higher density, lower temperature regions, are less influenced by photoionization from the UVB, as collisional ionization begins to dominate.

Throughout each comparison, it appears that the most significant differences are from comparisons with PW19. While it is reasonable that the comparison between HM12 would have some significant differences as PW19 has updated photoionization parameters and optimized effective rates from the HM12 background, the comparison between PW19 and FG20 does yield some interesting results as the differences between these two UVBs, namely in the H Icomparison, have very similar 3 dex differences between absorbers that also appear in the HM12-PW19 comparison. Upon further analysis, a comparison was performed between HM12 and FG20 was made, and there were no such 3 dex differences to be found in H I. I have a couple ideas as to why this is, but nothing concrete.

4.2. *Comparison to Other Literature*

As of late, works such as our own, focused on characterizing the uncertainties produced by the UVB have become a topic of much discussion as of late. The vast majority of which, focus on reverse modeling approaches to understand its complexities. One such work is from Lehner & Howk (2011), a study focusing that contributes to this discussion as well. This study focuses on allowing the power-law slope of the UVB vary as a free parameter. Doing so causes uncertainties in CGM ion column densities to increase from 0.08 to 1.14 dex. Our work shows a similar trend, with the majority of uncertainties (outside of H I) remaining within 1 dex.

Mallik et al. (2023) investigates a very similar topic to the one addressed within our work. In this paper, the authors perform both a forward and backward modeling approach, looking at the impact of UVB on simulated absorption features and their subsequently inferred column densities rather than directly looking at the absorbers themselves. Although this leads to more sources of uncertainty, it also produces results that are much more comparable to observation. Our work helps expand upon the findings of Mallik et al. (2023), showing that the uncertainty in metal absorbers exists not only through the forward-backward modeling approach taken in their paper, but within the distribution of absorbers themselves. Another work, Acharya & Khaire (2022), also finds similar results in their study. This work also employs reverse modeling techniques via the creation of "toy" absorbers, using CLOUDY to recover the H Inumber density and metallicity. Here, they find very similar results to our work, with the main differences being the authors only used H Iin their analysis and had a much more significant focus on inferred physical quantities as opposed to inferred column density. Regardless, our work also serves to extend the results of this paper, showing the variance between the different UVB models result in differences for multiple ion species in both forward modeling and backward modeling approaches. In opposition of these backward modeling approaches, Marra et al. 2024 finds that there is some caution to be had with this methodology and the assumption that all of the absorption features of a cloud originate from a singular absorber. In their work, they found that a significant portion of the features of absorption

spectra appear from sets of multiple absorbers, a significant portion of which do not share common gas mass. This serves to support our forward modeling approach as we are completely able to avoid introducing the uncertainty from this assumption into our analysis.

Another study that analyzes the CGM at $z \approx 2$, Lehner et al. (2022) analyzes the metalicity of CGM absorbers observed by KODIAQ-Z as compared to FOGGIE simulation data. To extract absorbers from the FOGGIE galaxies, the authors also use SALSA, using HM 2012 as the UV background for their analysis. Given the insights of our work the metalicity in their analysis would likely remain relatively unchanged, regardless of which UVB model was used. However, there would likely be some changes in the H Icolumn densities around $10^{18} - 10^{20}$ cm^{-2} range as more recent models have significantly lower gas densities of H I(≈ 0.5 dex) in this column density range.

4.3. *Limitations*

One drawback of this work stems from our direct analysis of absorbers that are physically contiguous, extracting their column densities rather than estimating the column density via absorption spectra. While our approach may not be the most conventional, the goal of this work is ultimately to compare impact of different UVB models, and the most direct way to understand the physical impacts is by looking at the absorbers themselves. In this way, we avoid any additional variables that may confuse the results of the analysis.

Additionally, the variables used in the iterative process of SALSA, cutoff fraction and minimum density are still arbitrarily selected, despite our efforts to calibrate them. Future work may consider calibrating these quantities against observational data to further increase accuracy. There is also the use of boolean logic in the absorber categorization script in which the margins of error for establishing these categories are set arbitrarily. This is further complicated by the random physical sizes of each cell along the randomly oriented ray objects (see sec 2) which lowers the accuracy of setting a single error margin based around ray cells as each ray cell is not the same size, nor are they the same size between different rays. Future studies should attempt to remedy these issues by instead setting an error region based around physical size rather than cell indices. Finally, our work has some inconsistencies as we are using temperature, density, metallicity values that come from using a specific UVB in the FOGGIE simulations (which one was it?), then post-processing them with different UV backgrounds. Unfortunately, this is the only way to perform absorber-by-absorber matching as rerunning entire simulations under different UVBs is far to computationally expensive to be feasible within the bounds of this project.

5. CONCLUSIONS

In this paper we have utilized CLOUDY to generate ionization tables from more recent UVB models, performed a psuedo-grid search to optimize the SALSA absorber extractor algorithm, generated 100 randomly-oriented rays through a simulated FOGGIE galaxy, utilized SALSA to extract absorbers from each ray under four different UVBs: FG 2009, FG 2020, HM 2012 and PCW 2019, ran an absorber-categorization algorithm to perform a pairwise sort through respective SALSA absorbers to categorize them and remove absorbers that could not be compared. Finally, we analyzed our results via a series of plots comparing the column density differences with gas density and temperature.

From our analysis, we found:

1. Observed column densities show significant differences between UVBs, with notable patterns between model generations and between model families

2. the differences between UVB are most significant in regions where they are the most effective (low density, high temperature)

3. our work agrees with much of the current literature that focused on backward modeling

There are several areas of uncertainty in this work that may be pursued in future works. Firstly, concerning variation in elemental abundances. We assume in this work that all gas, regardless of metallicity, has the Solar abundance ratios. This is not always true, and in fact we would expect that the (non-hydrogen) elements that are commonly observed in the CGM would have some variation in their relative abundance – carbon comes from both massive stars and low-mass stars, whereas oxygen and magnesium come entirely from massive stars, and even the elements that come from the same sources will not necessary end up with precisely the same ratios. Future work should attempt to re-evaluate these results under different abundance patterns that could potentially more accurately represent that which might be observed in the CGM. We also must consider the inclusion of the variation of the UV background near galaxies

due to the massive stars in that galaxy. This is potentially important at low impact parameters, and it likely also depend on the azimuthal angle – i.e., UV light from stars is going to preferentially escape along the poles rather than in the equatorial plane. Again, an area for future work. Lastly, as a next step towards approaching the synthesis of observational results, velocity blending of absorbers might be considered in future works. This is justifiable because we have constrained our analysis in a specific way, but if we were trying to get closer to observations, this would be an important factor.

Software: astropy (Astropy Collaboration et al. 2013, 2018), yt (Turk et al. 2011), Trident (Hummels et al. 2017), SALSA (Boyd et al. 2020)

APPENDIX

REFERENCES

Acharya, A., & Khaire, V. 2022, Monthly Notices of the Royal Astronomical Society, 509, 5559–5576, doi: 10.1093/mnras/stab3316

Astropy Collaboration, Robitaille, T. P., Tollerud, E. J., et al. 2013, A&A, 558, A33, doi: 10.1051/0004-6361/201322068

Astropy Collaboration, Price-Whelan, A. M., Sipőcz, B. M., et al. 2018, AJ, 156, 123, doi: 10.3847/1538-3881/aabc4f

Berg, M. A., Howk, J. C., Lehner, N., et al. 2019, doi: https://doi.org/10.3847/1538-4357/ab378e

Bordoloi, A. D., & Longmire, E. K. 2018, Physical Review Fluids, 3, doi: 10.1103/physrevfluids.3.123602

Bordoloi, R., Lilly, S. J., Kacprzak, G. G., & Churchill, C. W. 2014, ApJ, 784, 108, doi: 10.1088/0004-637X/784/2/108

Boyd, B., Silvia, D., O'Shea, B., et al. 2020, The Journal of Open Source Software, 5, 2581, doi: 10.21105/joss.02581

Butsky, I. S., Werk, J. K., Tchernyshyov, K., et al. 2022, The Astrophysical Journal, 935, 69, doi: 10.3847/1538-4357/ac7ebd

Chen, H.-W., Zahedy, F. S., Boettcher, E., et al. 2020, Monthly Notices of the Royal Astronomical Society, 497, 498

DeFelippis, D., Bouché, N. F., Genel, S., et al. 2021, The Astrophysical Journal, 923, 56, doi: 10.3847/1538-4357/ac2cbf

Faucher-Giguère, C.-A. 2020, MNRAS, 493, 1614, doi: 10.1093/mnras/staa302

Fielding, D., Quataert, E., McCourt, M., & Thompson, T. A. 2017, Monthly Notices of the Royal Astronomical Society, 466, 3810–3826, doi: 10.1093/mnras/stw3326

Gibson, J. L., Lehner, N., Oppenheimer, B. D., et al. 2022, The Astronomical Journal, 164, 9, doi: 10.3847/1538-3881/ac69d0

Haislmaier, K., Tripp, T., Katz, N., et al. 2020, Monthly Notices of the Royal Astronomical Society, 502, doi: 10.1093/mnras/staa3544

Hummels, C. B., Bryan, G. L., Smith, B. D., & Turk, M. J. 2013, Monthly Notices of the Royal Astronomical Society, 430, 1548–1565, doi: 10.1093/mnras/sts702

Hummels, C. B., Smith, B. D., & Silvia, D. W. 2017, ApJ, 847, 59, doi: 10.3847/1538-4357/aa7e2d

Hummels, C. B., Smith, B. D., Hopkins, P. F., et al. 2018, The Astrophysical Journal, 882, 156, doi: 10.3847/1538-4357/ab378f

Lehner, N., & Howk, J. C. 2011, Science, 334, 955–958, doi: 10.1126/science.1209069

Lehner, N., O'Meara, J., Fox, A., et al. 2014, The Astrophysical Journal, 788, doi: 10.1088/0004-637X/788/2/119

Lehner, N., O'Meara, J. M., Howk, J. C., Prochaska, J. X., & Fumagalli, M. 2016, ApJ, 833, 283, doi: 10.3847/1538-4357/833/2/283

Lehner, N., Wotta, C. B., Howk, J. C., et al. 2018, The Astrophysical Journal, 866, 33, doi: 10.3847/1538-4357/aadd03

Lehner, N., Kopenhafer, C., O'Meara, J., et al. 2022, The Astrophysical Journal, 936, 156, doi: 10.3847/1538-4357/ac7400

Mallik, S., Srianand, R., Maitra, S., Gaikwad, P., & Khandai, N. 2023, Monthly Notices of the Royal Astronomical Society, 523, 2296, doi: 10.1093/mnras/stad1550

Marra, R., Churchill, C. W., Kacprzak, G. G., et al. 2022, Examining quasar absorption-line analysis methods: the tension between simulations and observational assumptions key to modelling clouds. https://arxiv.org/abs/2202.12228

Marra, R., Churchill, C. W., Doughty, C., et al. 2021, MNRAS, 508, 4938, doi: 10.1093/mnras/stab2896

Peeples, M. S., Corlies, L., Tumlinson, J., et al. 2019, The Astrophysical Journal, 873, 129, doi: 10.3847/1538-4357/ab0654

Prochaska, J. X., Macquart, J.-P., McQuinn, M., et al. 2019, Science, 366, 231–234, doi: 10.1126/science.aay0073

Ramesh, R., Nelson, D., Fielding, D., & Brüggen, M. 2024, Astronomy amp; Astrophysics, 684, L16, doi: 10.1051/0004-6361/202348786

Schaye, J., Crain, R. A., Bower, R. G., et al. 2014, Monthly Notices of the Royal Astronomical Society, 446, 521–554, doi: 10.1093/mnras/stu2058

Simons, R. C., Peeples, M. S., Tumlinson, J., et al. 2020, ApJ, 905, 167, doi: 10.3847/1538-4357/abc5b8

Tumlinson, J., Thom, C., Werk, J. K., et al. 2011, Science, 334, 948–952, doi: 10.1126/science.1209840

Tumlinson, J., Thom, C., Werk, J. K., et al. 2013, ApJ, 777, 59, doi: 10.1088/0004-637X/777/1/59

Turk, M. J., Smith, B. D., Oishi, J. S., et al. 2011, ApJS, 192, 9, doi: 10.1088/0067-0049/192/1/9

Werk, J. K., Prochaska, J. X., Tumlinson, J., et al. 2013, The Astrophysical Journal, 792, 8, doi: 10.1088/0004-637x/792/1/8

Werk, J. K., Prochaska, J. X., Cantalupo, S., et al. 2016, The Astrophysical Journal, 833, 54, doi: 10.3847/1538-4357/833/1/54

Wijers, N. A., Schaye, J., & Oppenheimer, B. D. 2020, The warm-hot circumgalactic medium around EAGLE-simulation galaxies and its detection prospects with X-ray and UV line absorption. https://arxiv.org/abs/2004.05171

Wilde, M. C., Werk, J. K., Burchett, J. N., et al. 2021, The Astrophysical Journal, 912, 9, doi: 10.3847/1538-4357/abea14

Zheng, Y., Peeples, M. S., O'Shea, B. W., et al. 2020, The Astrophysical Journal, 896, 143, doi: 10.3847/1538-4357/ab960a